JOURNAL OF THERMOPHYSICS AND HEAT TRANSFER
Vol. 16, No. 3, July–September 2002

Parametric Analysis of Heat Transfer on Multistage Cryogenic Radiator

Paulo Couto* and Marcia B. H. Mantelli†
Federal University of Santa Catarina, 88040-900 Florianopolis, Brazil
E. E. Marotta‡
IBM Corporation, Inc., Poughkeepsie, New York 12601-5400
and
J. J. Fuller§
General Electric Power Systems, Greenville, South Carolina 29615

A theoretical and experimental parametric study of the heat-transfer phenomena on a multistage passive cryogenic radiator is presented. This investigation was performed in the frame of a cooperative effort between Clemson University and the Federal University of Santa Catarina. Passive cryogenic radiator technology is under development at the Satellite Thermal Control Laboratory at the Federal University of Santa Catarina, where two experimental prototypes have been built and ground tested. The mathematical model, developed to predict the temperature distribution on the radiator stages, was used to study the sensitivity coefficients with respect to the design parameters. The design parameters considered are the radiator stage's surface emissivity, the multilayer insulation effective emissivity, the radiator support's global conductance, and the thermal load over the radiator stages. This sensitivity analysis showed that the thermal joint conductance between the stages and the support structure (aluminum-Teflon®) plays an important role in the temperature distribution of the radiator. An experimental study was conducted within the Mechanical Engineering Department of Clemson University to gather thermal conductance data for comparison with the theoretical results. The thermal conductance data were incorporated into an analytical model developed for the prediction of the transient temperature behavior of a multistage cryogenic radiator for spacecraft applications. The data were also compared with the recently developed model for the prediction of thermal conductance of polymer and metal joints. Ultimately, conclusions are presented about the importance of the thermal conductance between the polymer support structure and the passive cryogenic radiator stages in the temperature distribution of the radiator.

Nomenclature

A	=	area, m^2
a	=	inner domain radius, m
b	=	outer domain/external radius, m
C_p	=	specific heat at constant temperature, J/kg K
E	=	Young modulus, Pa
h_c	=	theoretical joint conductance, W/m^2K
h_j	=	experimental joint conductance, W/m^2K
k	=	thermal conductivity, W/mK
L	=	low-conductance support length, m
m_{abs}	=	mean slope of the surface profile, rad
Q_{eq}	=	equipment heat load, W
q_{flux}	=	flux meter heat flux, W/m^2
q_i	=	heat balance at the stage i, W
r	=	radius, m
T	=	temperature, K
T_g	=	glass transition temperature, K
t	=	time, s; thickness of the elastic layer, mm
U	=	global conductance, W/K
X	=	sensitivity coefficient
α	=	thermal diffusivity, m^2/s; absorptivity
β_n	=	eigenvalues
δ	=	thickness, m
ε	=	emissivity
Θ	=	nondimensional temperature
ρ	=	density, kg/m^3
σ	=	Stefan–Boltzmann constant, W/m^2K^4; rms roughness, m
τ	=	time-integration factor, s

Subscripts

a, b	=	inner and outer sun shield radius
in, out	=	inner and outer intermediate stages domains
sl	=	lower surface
su	=	upper surface

Received 14 March 2001; revision received 20 November 2001; accepted for publication 3 December 2001.

*Engineer/Researcher, Department of Mechanical Engineering, P.O. Box 476; currently Exchange Visitor, Mechanical Engineering Department, Clemson University, 121 Fluor Daniel Building, Clemson, SC 92634-0921; couto@labsolar.ufsc.br. Member AIAA.

†Professor, Department of Mathematics, P.O. Box 476; marcia@emc.ufsc.br. Member AIAA.

‡Senior Engineer/Scientist, Thermal Technologies—PPP&C; egidio1@us.ibm.com. Senior Member AIAA.

§Thermal Engineer; Jason.Fuller@ge.ps.com. Student Member AIAA.

Introduction

THE thermal control of a satellite in orbit is usually achieved by balancing the thermal energy dissipated by the internal electronic equipment and the energy absorbed from its environment. Because convenction heat transfer does not exist in a space environment, the heat-transfer mechanisms that control this balance are conduction and radiation. The temperature ranges in which satellite components operate are usually narrow. Therefore, more heat is transferred by conduction through the spacecraft structure than transferred by radiation inside the compartments. So, conduction heat transfer is the most effective means of thermal control of electronic equipment aboard satellites.

Electronic equipment, such as infrared (IR) sensors and charged-coupled devices (CCD) cameras, usually operate at cryogenic temperature levels. Because of their operating temperature, they require good thermal decoupling while maintaining good mechanical coupling to the satellite structure. This type of attachment can be achieved by means of low-conductance supports[1] or variable thermal resistance devices[2] (heat switches). Additionally, thermal control devices that provide the required cooling for these equipments are needed. The passive cryogenic radiator is one of these satellite thermal control devices, which takes the waste thermal energy from one source and discharges it by radiation into deep space. The source is usually the electronic components. It is essential that these electronic components be kept at their correct operating temperature to maintain optimum performance in orbit. This requirement becomes paramount when one considers that the surrounding temperature can vary from several degrees above absolute zero to 300 K. In theory, passive cryogenic radiators can be employed to reduce component temperatures down to 60 K, and their greatest asset is their simplicity of design and its independence from an external power source. Actually, below 100 K the radiator heat rejection capacity falls dramatically.

Passive cryogenic radiators are used for cooling CCD and IR cameras[3,4] and x-ray telescopes,[5] among many other types of electronic equipment. The heat load is transferred from the source to the radiator stages through direct contact,[6] fluid loops,[7] phase change materials,[8] or heat pipes.[4,9–12] Passive cryogenic radiators can have one stage (single-stage) or more than one stage (multistages). The principle of operation of a multistage radiator, given by Wilson and Wright,[11,12] is based on an efficient thermal insulation among the stages by means of a multilayer insulation (MLI) and low-conductance supports, which minimize heat exchange by radiation and by conduction, respectively. On the other hand, low-conductance supports can also provide high mechanical coupling needed during the launch/ascent phase of the mission. Each intermediate stage intercepts the parasitic heat leakage from the insulation below and radiates it to space, thus allowing the successive radiator stages to achieve colder temperatures. The lowest temperature stage is called the radiator cold stage, which dissipates the waste thermal energy. Usually, the radiator stages are shielded from environmental heat sources, such as solar radiation, terrestrial infrared, and albedo radiation, by means of a sun shield. The sun shield reflects back the environmental heat load into space, therefore, providing insulation to the radiator cold plate, as shown in Fig. 1.

Many parameters must be considered for the design of passive cryogenic radiators. These parameters include the optical properties of the radiator stages and of the MLI, thermal properties of the insulating materials, heat load applied to the radiator cold plate, and geometry. Couto and Mantelli[13] presented the area/temperature optimization procedure for a small-scale passive cryogenic radiator. This optimization procedure was based on geometric parameters. They proposed three prototypes: one, two, and three stages. The optimized areas for the stages are shown in Table 1. Figure 2 shows the proposed triple-stage radiator prototype mounted with the sun shield, MLI, and thermocouples. One can notice that the internal surface of the sun shield has a high reflectivity finishing, thus providing directional reflection of the environmental heat loads. Also,

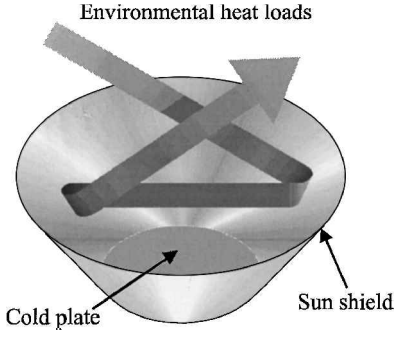

Fig. 1 Configuration of a passive cryogenic radiator.

Table 1 Passive cryogenic radiator optimum areas[13]

Stage	Single stage, m^2	Double stage, m^2	Triple stage, m^2
1st stage[a]	0.02270	0.01584	0.01674
2nd stage	——	0.00686	0.00387
3rd stage	——	——	0.00209
Total area	0.02270	0.02270	0.02270

[a]Cold stage.

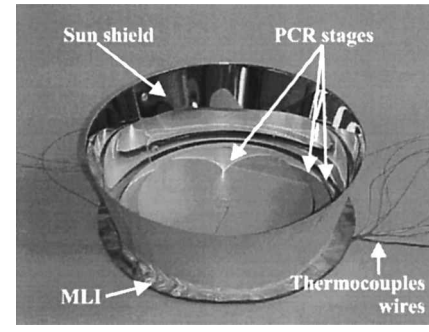

Fig. 2 Proposed configuration for the multistage passive cryogenic radiator.[13,15]

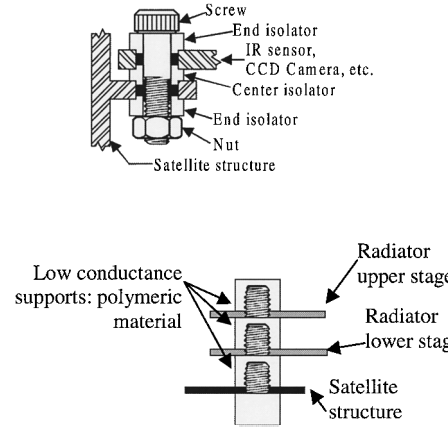

Fig. 3 Examples of low-thermal-conductance support systems for spacecraft application: IR sensor (or CCD camera) attachment to the satellite structure (top) and radiator panels fixation (bottom).

the upper surface of the stages is painted with high emittance white paint, which improves the heat-rejection capacity of the cold plate and intermediate stages.

To develop a procedure for the radiator design optimization, a parametric analysis of the heat-transfer phenomena on the stages of a passive cryogenic radiator was required. This paper deals with this analysis. The sensitivity coefficients[14] with respect to each of the design parameters are presented. These parameters are the radiator stages surface emissivity ε_R, multilayer insulation effective emissivity ε_{MLI}, radiator supports global conductance U_s, and thermal load over the radiator stages Q_{eq}. The analytical expressions for the temperature distribution for each stage, developed by Couto[15] and Couto and Mantelli[16] were used to derive these coefficients. The global conductance of the supports considered by these authors is defined as

$$U_s = 1/(1/h_{c,\text{inf}} + L/k + 1/h_{c,\text{sup}}) \tag{1}$$

where $h_{c,\text{inf}}$ is the contact conductance between the lower stage and the support, L/k is the thermal resistance of the support, and $h_{c,\text{sup}}$ is the thermal contact conductance of the support and the upper stage. Figure 3 presents a few examples of low-conductance supports employed in spacecraft applications.

The thermal contact conductance h_c between Teflon®/metal joints at cryogenic temperatures, which determines the global conductance of the supports [Eq. (1)], was experimentally determined to confirm

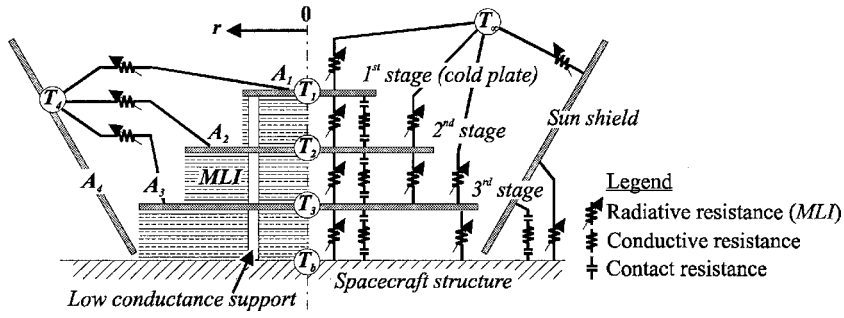

Fig. 4 Thermal resistance network for the triple stage PCR configuration.

the results of the parametric study. Couto and Mantelli[16] used Teflon as low-conductance support in a small-scale passive cryogenic radiator (PCR) that operates at 150 K. The authors concluded that the contact conductance between the supports and the radiator panels played an important role on the temperature level of the PCR components. Couto and Mantelli[16] did not measure this parameter. Instead, they used an average value for the temperature obtained between two extreme cases: a contact conductance tending to zero and an infinite contact conductance. When the contact conductance tends to zero, Eq. (1) becomes $U_s = 0$. This means that no heat passes through the interface of the support and the stages. When the contact conductance tends to infinity, Eq. (1) becomes $U_s = k/L$. This means that the contact between the support and the stages is perfect (no contact resistance). The temperature distribution was obtained by using the mathematical model with these two extreme limits ($U_s = 0$ and k/L), and then the average temperature between these two limiting cases was considered for comparison with experimental temperature data. This average temperature corresponds to a contact conductance of roughly $h_c = 102$ W/m^{2}K. The contact conductance obtained using experimental data is input into the mathematical model was shown to be of the same magnitude.

Recently, Fuller and Marotta[17] developed a thermal joint conduction model to predict the thermal conductance through a metal/polymer joint. The model includes both the microscopic and bulk properties of the joint to predict the heat transfer across the contact region. For the microscopic conductance portion, two models were proposed. One assumes deformation of asperities on a rigid, flat surface, and the other model is a rigid indenter in contact with an elastic layer. The model for the bulk conductance also accounts for the compressibility of the polymer layer caused by loading. The thermal joint model compared quite favorably to a limited amount of published data, and future directions in the modeling of a metal/polymer joint were proposed. A comparison between the thermal joint model developed by Fuller and Marotta[17] with experimentally gathered data at cryogenic temperatures would further enhance its creditability. Furthermore, greater insights could be ascertained for applicability of the Mikic[18] elastic thermal contact model at cryogenic temperatures.

The experimental setup described in this paper reproduces the same configuration used by Couto and Mantelli[16] for the PCR stage supports. The main objective of this work is to present the parametric analysis and to show whether the assumption of an average value of the two extreme cases was appropriate for determining the temperature distribution for the stages of a PCR. Therefore, on the basis of the analytical and experimental study conducted by Couto and Mantelli,[16] this study experimentally measures the thermal contact conductance between the support structure Teflon material and the radiator stage aluminum material, which simulates the contact conditions that exist for PCR devices.

Previous Works

Numerous investigators (Hulett and Ziermann,[1] Brand and Schlitt,[5] Merrian and Gabron,[6] Gilmore,[8] Wright and Pence,[9] Mayer,[19] and Gayrard[20]) have studied several PCR designs. Their thermal analyses were conducted with the use of commercially available computational packages. Couto and Mantelli,[16] however, developed a one-dimensional transient analytical model for the prediction of the temperature distribution of their particular PCR device using the Green Function Solution Equation (GFSE) method. The following assumptions have been made: 1) constant temperature on the PCR base plate (spacecraft structure) $T_b = 300$ K; 2) space temperature $T_\infty = 4$ K; 3) each PCR stage and the sun shield are at constant temperature at $t = 0$; and 4) the optical and physical properties are temperature invariant. The solution using the GFSE is given by[21]

$$\Theta_i(r,t) = \frac{\alpha}{k}\int_{\tau=0}^{t}\int_{r'=0}^{b_i}\frac{q_i}{\pi A_i \delta b_i^2}\left\{1+\sum_{n=1}^{\infty}\exp\left[\frac{-\beta_n^2\alpha(t-\tau)}{b_i^2}\right]\right.$$

$$\left.\times\frac{J_0(\beta_n r/b_i)J_0(\beta_n r'/b_i)}{J_0^2(\beta_n)}\right\}2\pi r'\,\mathrm{d}r'\,\mathrm{d}\tau \qquad (2)$$

where the β_n are obtained from $J_1(\beta_n) = 0$ and b_i is the external radius of the stage i.

The q_i term on Eq. (2) represents the combination of the heat exchange among the stages, the heat transfer between the stages and deep space, equipment heat load, and environmental heat loads (see scheme on Fig. 4). This term, given by Eq. (3), depends on the temperatures of each stage, which is unknown:

$$q_i = \left\{\begin{bmatrix}\text{Equipment}\\ \text{heat}\\ \text{load}\end{bmatrix} + \begin{bmatrix}\text{Parasitic}\\ \text{heat leakage}\\ \text{entering the stage}\end{bmatrix}_{\substack{\text{radiative and}\\ \text{conductive}}}\right\}$$

$$-\left\{\begin{bmatrix}\text{Parasitic}\\ \text{heat leakage}\\ \text{leaving the stage}\end{bmatrix}_{\substack{\text{radiative and}\\ \text{conductive}}} + \begin{bmatrix}\text{Heat}\\ \text{dissipated}\\ \text{to space}\end{bmatrix}\right\} \qquad (3)$$

To obtain the temperature distribution, temperatures are assumed for each stage, and the heat loads are calculated. Based on these heat loads, the temperature distribution was determined. The average temperature for each stage and sun shield was calculated, and then the heat rate q_i term was obtained. The temperatures are determined again and compared with the input temperatures. This process continues until convergence was achieved.

Equations (4–6) show the heat balance of Eq. (3) written for the double-stage configuration radiator. In these equations $Q_{\text{eq},1}$ is the equipment heat load to be dissipated by the cold plate; ε_{MLI} and ε_R are the MLI and the stage surface emissivities, respectively; α is the stages surface absorptivity; T_1, T_2, and T_4 are the cold plate, second-stage, and sun-shield temperatures; T_b is the PCR base plate temperature (spacecraft structure); U_s is the global conductance of the low-conductance supports; and F_{41} and F_{42} are the view factors between the sun shield and the cold plate, and the sun shield and the second stage, respectively. The parameter U_s includes the contact resistance of the radiator stages and the low-conductance supports:

$$q_1 = \left\{Q_{\text{eq},1} + \sigma\varepsilon_{\text{MLI}}A_1\left(T_2^4 - T_1^4\right) + U_s(T_2 - T_1)\right.$$

$$\left.+\alpha\left[\sigma\varepsilon_4 A_4 F_{41}\left(T_4^4 - T_1^4\right)\right]\right\} - \left[\sigma\varepsilon_R A_1\left(T_1^4 - T_\infty^4\right)\right]$$

$$\text{in}\quad 0 \le r \le b_1 \qquad (4)$$

$$q_{\text{ext},2} = \left\{\sigma\varepsilon_{\text{MLI}}A_2\left(T_b^4 - T_2^4\right) + \alpha\left[\sigma\varepsilon_4 A_4 F_{42}\left(T_4^4 - T_2^4\right)\right]\right\} - \left[\sigma\varepsilon_R A_2\left(T_2^4 - T_\infty^4\right)\right] \quad \text{in} \quad a_2 \le r \le b_2 \quad (5)$$

$$q_{\text{in},2} = \left[Q_{\text{eq},2} + \sigma\varepsilon_{\text{MLI}}A_1\left(T_b^4 - T_2^4\right) + U_s(T_b - T_2)\right] - \left[\sigma\varepsilon_{\text{MLI}}A_1\left(T_2^4 - T_2^4\right) + U_s(T_2 - T_2)\right] \quad \text{in} \quad 0 \le r < a_2 \quad (6)$$

For the cold plate the integral on the right-hand side of Eq. (2) is evaluated over its whole domain ($r' = 0$ through b_1). For the intermediate stages this integral is evaluated over the inner domain ($r' = 0$ through a_i) and the outer domain ($r' = a_i$ through b_i).

Figures 5 and 6 show the comparison between theoretical results, using the present model, and experimental data for the double- and the triple-stage configuration radiator, respectively. The vertical bars over the experimental data represent the experimental uncertainties. The continuous line represents the theoretical temperature variation considering an infinite contact conductance ($U_s = k/L$) between the radiator stages and its supports. The dotted lines represent the theoretical temperature variation considering a contact resistance tending to zero ($U_s = 0$). These lines represent the two extreme cases discussed in the preceding section. The present authors believe that the contact conductance is zero or infinite. The arithmetic mean temperature between the extreme limiting cases was considered. The point-dotted line represents this average.

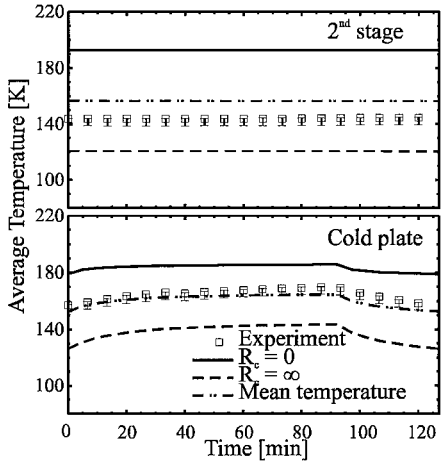

Fig. 5 Temperature variation as a function of time for the double-stage PCR.

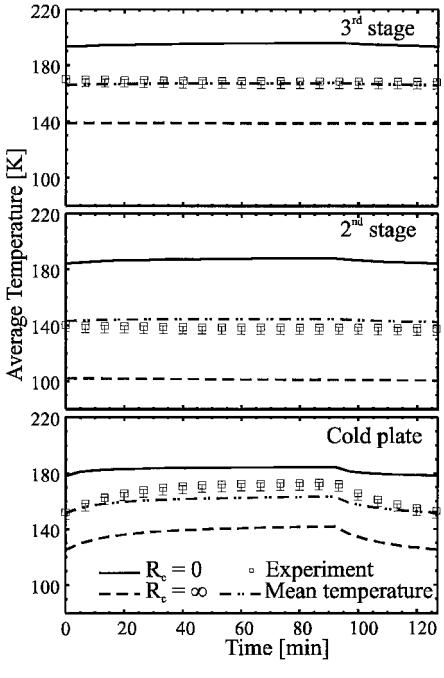

Fig. 6 Temperature variation as a function of time for the triple-stage PCR.

Two levels of heat load applied to the cold plate were considered in Figs. 5 and 6. The first level, applied over the time range $0 < t < 96$ min, corresponds to the sunny portion of the orbit, where the radiator is subjected to direct solar irradiation. This period is also named the "hot case." The second level, applied over the time range $96 < t < 127$ min, corresponds to the Earth eclipse. This is the "cold case." The orbit considered is circular ($0 < t < 127$ min), equatorial, and with an altitude of 2000 km. The experimental setup is discussed by Couto et al.[22]

Analysis of the Sensitivity Coefficients

The sensitivity coefficient is defined as the first derivative of a dependent variable, such as the stages temperature $T_i(r, t)$, with respect to an unknown parameter,[14] say, p:

$$X(r, t) \equiv \frac{\partial T_i(r, t)}{\partial p} \quad (7)$$

The sensitivity coefficient can be calculated as a function of time and position [$X = X(r, t)$], as a function of time only [$X = X(t)$], as a function of position only [$X = X(r)$], or as a function of a parameter at a given time and position [$X = X(p)$]. The parameter p can be, for example, the effective emissivity of the multilayer insulation. For instance, an optimal radiator is the one that is able to dissipate the largest amount of heat for a given radiator area. The study of the sensitivity coefficients leads to an overview of the parameters, which affect more the temperature distribution, and therefore the heat rejection capacity of a radiator.

For the present case, based on the mathematical model of Couto and Mantelli,[16] it is not posible to obtain an explicit expression for $T_i(x, t)$ because it depends on q_i, given by Eqs. (4–6), which, in turn, depends of $T_i(x, t)$. Therefore, the sensitivity coefficients are evaluated using a numerical central difference method. As shown by Eq. (8), the derivative of the temperature with respect to some parameter p at the point $p = p_m$ is the difference between the temperatures evaluated at the points $p_1 = p_m + \Delta p/2$ and $p_2 = p_m - \Delta p/2$, where Δp is small to avoid numerical oscillations:

$$X \equiv \frac{\partial T_i(r, t)}{\partial p} \cong \frac{T_i|_{p_1} - T_i|_{p_2}}{\Delta p} \quad (8)$$

The design parameters considered are the effective emissivity of the multilayer insulation ε_{MLI}, the surface emissivity of the radiator stages ε_R, the global conductance of the radiator supports U_s, and the thermal heat load over the radiator cold plate $Q_{\text{eq},1}$. The analyzed parameters and the range of variation of the values used are shown in Table 2.

The nondimensional sensitivity coefficients for these parameters are defined as follows: 1) sensitivity coefficient for the effective emissivity of the multilayer insulation

$$X_{\varepsilon_{\text{MLI}}} \equiv \left(\frac{\varepsilon_{\text{MLI,max}} - \varepsilon_{\text{MLI,min}}}{T_\infty - T_0}\right)\frac{\partial \bar{T}_i}{\partial \varepsilon_{\text{MLI}}} \quad (9)$$

Table 2 Analyzed parameters and intervals of differentiation

Parameter p	$p_{\max}$	$p_{\min}$	Δp
Effective MLI emissivity ε_{MLI}	0.5	0.0	0.002
Surface emissivity ε_R	1.0	0.5	0.002
Global conductance U_s	0.5	0.0	0.002
Equipment heat load Q_{eq}	1.0	0.0	0.005

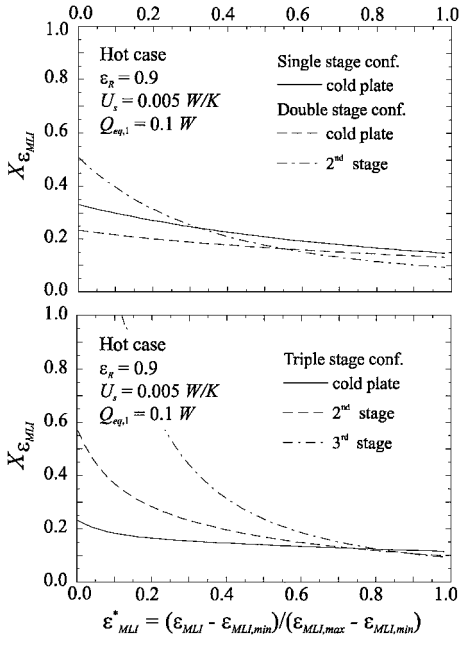

Fig. 7 Sensitivity coefficient for the effective emissivity of the MLI: $\varepsilon_{\mathrm{MLI}}$, hot case.

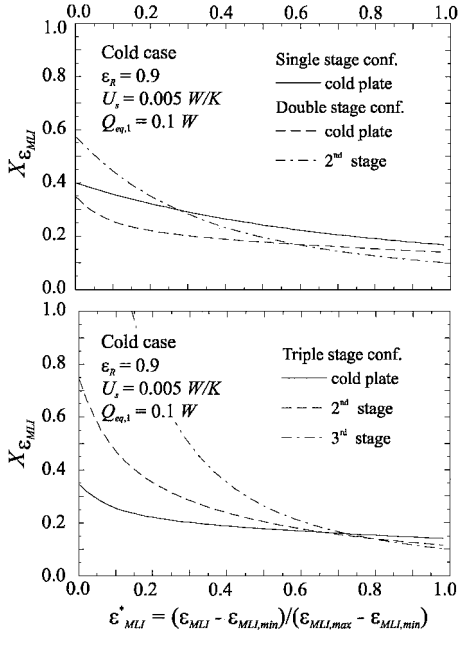

Fig. 8 Sensitivity coefficient for the effective emissivity of the MLI: $\varepsilon_{\mathrm{MLI}}$, cold case.

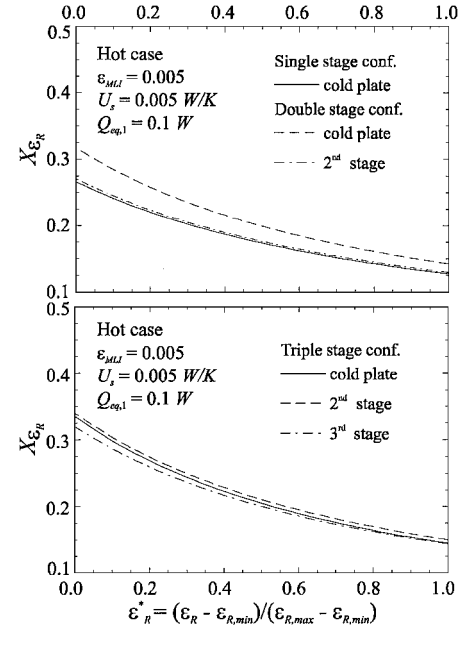

Fig. 9 Sensitivity coefficient for the surface emissivity of the stages: ε_R, hot case.

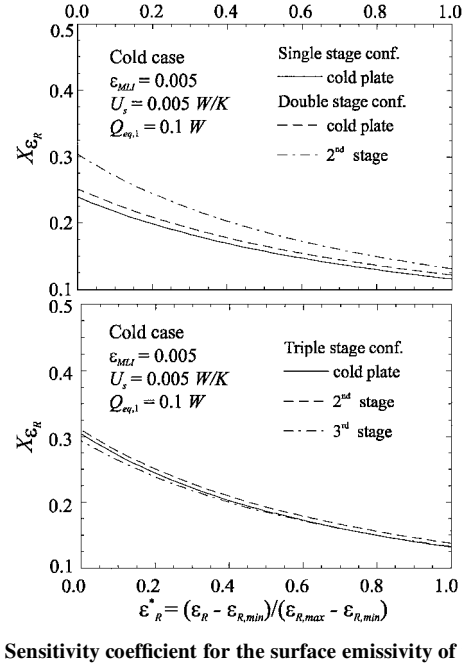

Fig. 10 Sensitivity coefficient for the surface emissivity of the stages: ε_R, cold case.

2) sensitivity coefficient for the surface emissivity of the radiator stages

$$X_{\varepsilon_R} \equiv \left(\frac{\varepsilon_{R,\max} - \varepsilon_{R,\min}}{T_\infty - T_0}\right)\frac{\partial \bar{T}_i}{\partial \varepsilon_R} \tag{10}$$

3) sensitivity coefficient for the global conductance of the radiator supports

$$X_{U_s} \equiv \left(\frac{U_{s,\max} - U_{s,\min}}{T_\infty - T_0}\right)\frac{\partial \bar{T}_i}{\partial U_s} \tag{11}$$

4) sensitivity coefficient for the thermal heat load over the radiator cold plate

$$X_{Q_{\mathrm{eq}}} \equiv \left(\frac{Q_{\mathrm{eq},\max} - Q_{\mathrm{eq},\min}}{T_\infty - T_0}\right)\frac{\partial \bar{T}_i}{\partial Q_{\mathrm{eq}}} \tag{12}$$

where $\bar{T}$ is the average temperature for the stage i, calculated for the steady-state condition at the hot and cold cases; T_∞ is the temperature of the space, and T_0 is the initial temperature of the radiator. The maximum and minimum values for the parameters used are listed in Table 2.

The hot and cold cases are analyzed. Figures 7–14 show the sensitivity coefficients for the hot and cold cases, as a function of the related parameters.

Figures 7 and 8 show the sensitivity coefficient for the effective emissivity of the multilayer insulation for the single-, double-, and triple-stage configurations proposed by Couto and Mantelli[13,16] for the hot and cold cases, respectively. This coefficient is plotted against a normalized emissivity ($\varepsilon^*_{\mathrm{MLI}}$), defined as $\varepsilon^*_{\mathrm{MLI}} = (\varepsilon_{\mathrm{MLI}} - \varepsilon_{\mathrm{MLI,min}})/(\varepsilon_{\mathrm{MLI,max}} - \varepsilon_{\mathrm{MLI,min}})$, where $\varepsilon_{\mathrm{MLI,max}}$ and $\varepsilon_{\mathrm{MLI,min}}$ are given in Table 2. It can be observed that the stage temperatures are more sensitive to the $\varepsilon^*_{\mathrm{MLI}}$ variations for $\varepsilon^*_{\mathrm{MLI}} < 0.4$ for both hot and cold cases. Also, $\varepsilon^*_{\mathrm{MLI}}$ affects the third stage more than the cold plate and second stage. This is because the amount of radiative parasitic heat load that passes through the MLI between the

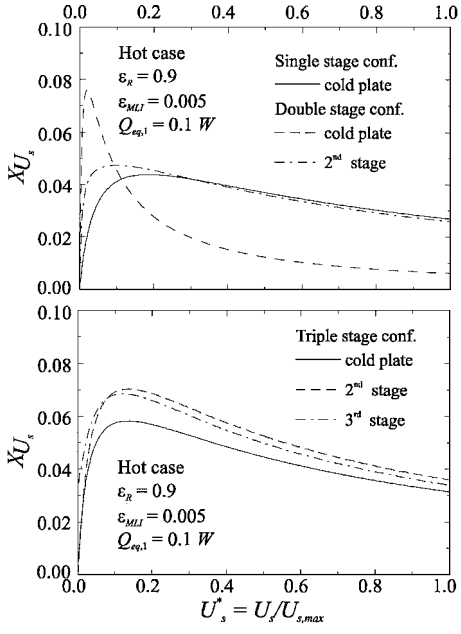

Fig. 11 Sensitivity coefficient for the global conductance of the stage supports: U_s, hot case.

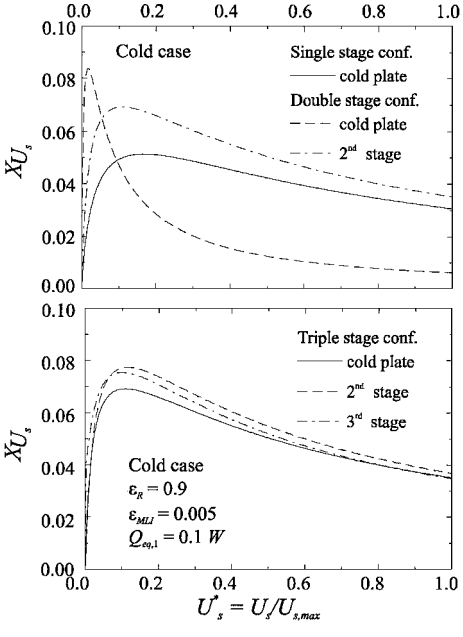

Fig. 12 Sensitivity coefficient for the global conductance of the stage supports: U_s, cold case.

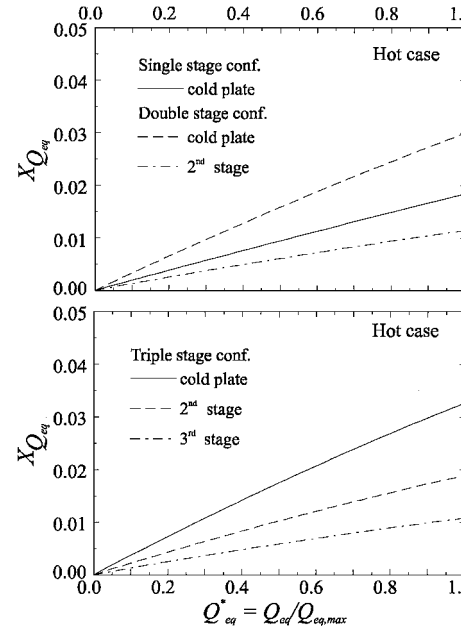

Fig. 13 Sensitivity coefficient for the equipment heat load over the cold plate: Q_{eq}, hot case.

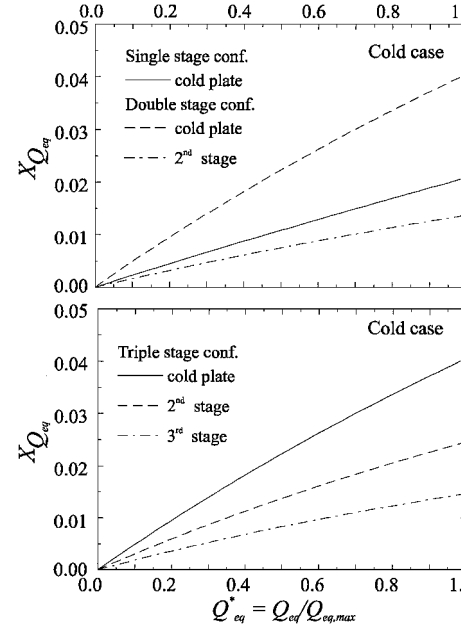

Fig. 14 Sensitivity coefficient for the equipment heat load over the cold plate: Q_{eq}, cold case.

third stage and the satellite structure (radiator's base, which is kept at 300 K) is larger than those between the third and the second stage and those between the second stage and the cold plate. Comparing both plots in Fig. 7, one can see that the cold plate of the single-stage radiator is more sensible to variations of $\varepsilon^*_{\mathrm{MLI}}$ than the cold plate of the double- and triple-stage configurations. This is because the intermediate stages on the double- and triple-stage configurations intercept the parasitic heat leakage from the stages below and irradiate it to the space, decreasing the total amount of parasitic heat load that impinges the cold plate. The $X\varepsilon_{\mathrm{MLI}}$ for the cold plate of the double- and triple-stage configurations present almost the same behavior.

Comparing Figs. 7 and 8, one can see that the temperature of the stages are more sensitive to variations in the effective emissivity of the MLI in the cold case than in the hot case. This is because the temperature level in which the radiator stages operate in the cold case is lower than that in the hot case. Therefore, even though there is no direct radiation from the sun impinging the sun shield of the radiator the radiative parasitic heat load that passes through the MLI between the spacecraft structure and the radiator's stages can effectively affect the temperature of these stages when compared to the hot case.

Figures 9 and 10 show the temperature sensitivity coefficient for the surface emissivity of the stages, for the single-, double-, and triple-stage configurations for the hot and cold cases, respectively. This coefficient is plotted against a normalized emissivity ε^*_R, similar to $\varepsilon^*_{\mathrm{MLI}}$. In these figures one can see that the variation of the stage temperatures is almost linear with the surface emissivity. According to Fig. 5, the experimental temperature data of the second stage is lower than the temperature of the cold plate for the whole orbit period. The same effect occurs in the triple-stage configuration (see Fig. 6). This is because there is no equipment heat load applied to the second stage.[16] The lowest temperature level in the second stage for the triple-stage configuration explains the fact that the second stage

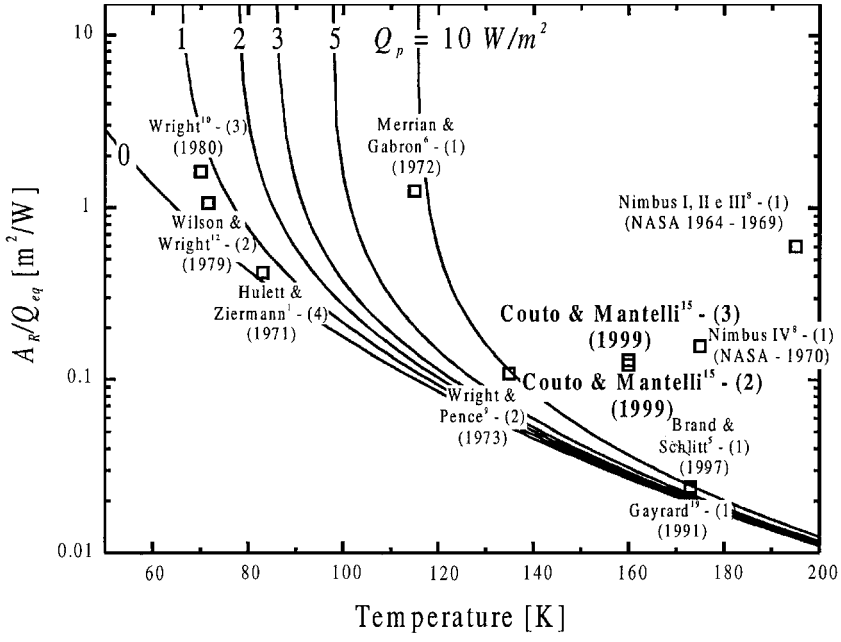

Fig. 15 Comparison between the experimented prototypes and existing devices.[16]

is more sensitive to variations in the surface emissivity than the cold plate. The cold plate of all of the configurations is more sensitive in the hot case than in the cold case. This is because the temperature difference between the cold plate and the space is smaller in the cold case than in the hot case. So, in the hot case variation in the surface emissivity enables the cold plate to irradiate more heat than for the cold case.

Figures 11 and 12 shows the sensitivity coefficient for the global conductance of the stage supports for the hot and cold cases, respectively. This coefficient is plotted against a nondimensional conductance U_s^*, defined similarly to $\varepsilon_{\text{MLI}}^*$. It is shown that the global conductance of the stage support plays an important role in the determination of the temperature of the stages. For values of U_s^* varying from 0 to around 0.1, the sensitivity coefficient increases sharply. This can be understood by examining the parasitic heat that passes through the support by conduction. Low values for U_s prevent this parasitic heat leakage so that the stages can achieve lower temperature levels. At this temperature level the temperatures of the stages are very sensitive to small changes on the support global conductance. One way to achieve low values of U_s is to use low-conductance supports with a high thermal contact resistance between the radiator stages, such as the heat switch shown by Milanez and Mantelli.[2] At U_s^* around 0.1, the sensitivity coefficient achieves a maximum, showing that, at this point, small variations in the global conductance of the supports can lead to large variations in the temperature level of the stages. For values of U_s^* larger than 0.1, the sensibility coefficient decreases smoothly. In this range of U_s^*, the parasitic heat load by conduction that passes through the supports is effective enough to keep the temperature of the stages at a high level. So, small changes in this parameter will not change effectively the temperature of the stages. This means that an optimum value for the global conductance of the supports exists. If U_s is too low, the temperature of the cold plate tends to be higher than the temperature of the second stage. If U_s is too large, the temperature of all of the stages tends to increase.

An interesting effect occurs in the double-stage configuration: at $U_s^* \sim 0.09$ the curves of the sensitivity coefficient for the cold plate and the second stage cross each other, and this is observed both in the hot and in the cold cases. This occurs because when the equipment heat load is imposed to the cold plate, the temperature of the cold plate tends to increase. For this case, according to Fig. 5, the temperature of the cold plate is larger than the temperature of the second stage. So, heat is conducted back from the cold plate to the second stage by the supports. An increase of the global conduction of the supports will make the temperature of the second stage increase while the temperature of the cold plate decreases. If the conductance of the supports passes the crossing point of Fig. 11, both temperatures (second stage and cold plate) will increase. The same effect occurs in the triple-stage configuration (see Fig. 6 in preceding section and Fig. 12) but in a smoother way.

Figures 13 and 14 show the influence of the heat load applied to the cold plate over the temperature of the stages. One can see that the cold plate is the most sensitive stage of the radiator. This was expected once the equipment heat load is applied at this stage. The heat that is conducted by the supports and irradiated through the MLI back to these stages affects the temperature level of the other stages. The radiator stages are more sensitive in the cold case than in the hot case. This is as a result of the lowest temperature level found in the former than in the latter.

Figure 15, obtained from Couto and Mantelli,[16] presents the comparison between the experimented prototypes and the existing devices in the literature. The cold-plate area/equipment heat load (A_r/Q_{eq}) ratio is plotted against the cold-plate temperature. different levels of parasitic heat loads are presented (Q_p). The number into brackets represents the number of stages of the device tested. According to the results of the sensitivity coefficient analysis, the performance of the two prototypes can be improved by improving the radiative and conductive insulation between the stages to decrease the level of parasitic heat load. So the prototypes would be able to operate at temperatures around 100 K for the same A_r/Q_{eq} level.

The parametric analysis showed that the global conductance of the stages is an important parameter on the determination of the temperature distribution of the passive cryogenic radiator. Although the model had compared well with experimental data, the contact conductance was not modeled. This is because there were no models for the contact conductance of polymer/metals interface available in the literature at the time the PCR mathematical model was developed. Experimental data for the contact conductance were required for comparison with the PCR model. The experimental setup and the comparisons are described in the following sections.

Experimental Facility

To obtain experimental thermal conductance data on Teflon at cryogenic temperatures, an experimental program was conducted, which is similar to that of Marotta and Fletcher.[23] A schematic of the experimental apparatus is shown in Fig. 16.

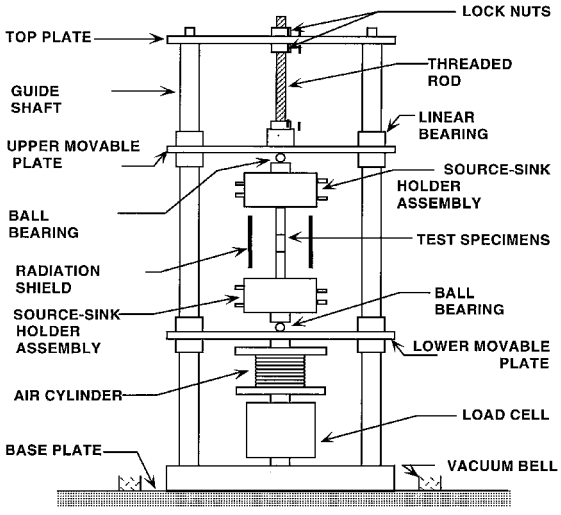

Fig. 16 Experimental facility.

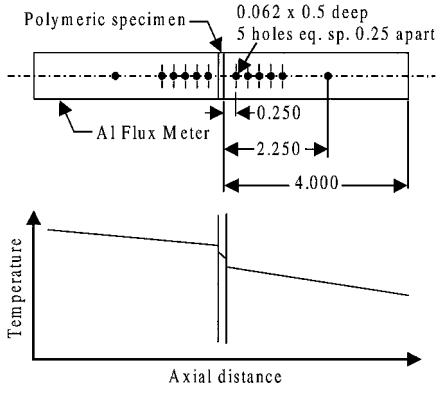

Fig. 17 Schematic of the experimental stack.

The experimental apparatus was housed in a vacuum bell and maintained at a low pressure of 1×10^{-5} bar (1 Pa) using a Welch Duo-Seal® rotary vacuum pump. The pressure was monitored using a pressure transducer connected to an Alcatel TA111 indicator.

The experimental apparatus consists of a vertical stack that contains three vertical stainless-steel columns mounted with two movable Teflon plates on linear bearings. An applied load to the experimental stack was controlled using a Bimba Flat-1® air cylinder, and the applied load was measured using on OMEGA LCHD-1K low-profile load cell wired to an OMEGA DP41-S high-performance strain gauge indicator. Uniform loading of the test section was ensured by the use of two hardened stainless-steel balls that transferred the load from the vertical column to the source/sink assemblies.

The experimental stack consisted on an upper and lower Aluminum 6061 flux meter and the polymer specimen. A schematic of the experimental stack is shown in Fig. 17. Each flux meter was housed in a fabricated source/sink holder. A Watlow Thinband® 500-W band heater encompassed the upper source holder. Circulating high-pressure liquid nitrogen through the chiller block cooled the lower sink holder.

It was important to have an accurate value for the thermal conductivity of the Al flux meters at cryogenic temperatures; therefore, the thermal conductivity of the Al 6061 flux meters was calibrated by using National Institute of Standards and Technology (NIST) iron samples. A NIST iron sample was used at the upper flux meter and Al was used for the lower flux meter. By calculating the heat flux through the NIST flux meter, the temperature difference in the Al flux meter, and the average temperature of the Al flux meter, A plot for the thermal conductivity of Al as a function of temperature was generated. A plot of the thermal conductivity of Al as a function of temperature is shown in Fig. 18.

Table 3 Material characteristics

Characteristic	Al 6061	Teflon
t, mm	——	1.89
σ, m	5.11×10^{-7}	6.22×10^{-7}
k, W/m-K	146.2	0.25[a]
m, rad	0.27	0.235
E, MPa	72×10^{3}[b]	1.35×10^{2}[c], 2.76×10^{3}[d]

[a] Marotta and Fletcher at 300 K.[23]
[b] Measured at room temperature (293 K).
[c] Askeland.[24]
[d] Van Krevelen ($T < T_g$).[25]

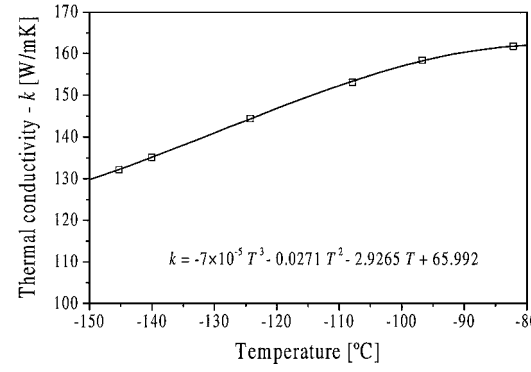

Fig. 18 Thermal conductivity of aluminum 6061 as a function of specimen temperature.

Sample Preparation

The flux meters and the polymer specimen were all cut to a diameter of 2.54 cm (1 in.). The Al flux meters were equipped with six 30-gauge "special limit of error" T-type thermocouples that were placed at the centerline.

The polymeric specimen was first machined into a 2.54-cm (1-in.)-diam rod. A Buehler ISOMET 2000 cutting tool was used to cut specimens to approximately 2-mm thickness. To ensure a nominally flat surface, both surfaces of the specimen were then polished using an EXAKT grinding wheel. The thickness of the specimen was measured at five different locations to ensure an uncertainty in the thickness of ± 0.005 mm.

The surface characteristics (rms roughness and average asperity slope) of the flux meters and polymeric specimen were measured using a WYKO NT-2000 noncontact surface profilometer with a magnification of 50x. Measurements were taken at five different positions on the surface and then averaged to ensure uniformity of the values. Material characteristics for the Al flux meter and the polymeric specimen are shown in Table 3 (Refs. 23–25).

Experimental Procedure

Joint-conductance values were experimentally measured between the flux meters and the polymer specimen over an interface pressure range of 138–4137 kPa (20–600 psi). The average specimen temperature of the polymeric material was maintained at -80°C (193.15 K) throughout the experiment while the interface temperature between the aluminum 6061 flux meter and the Teflon specimen was maintained at -150°C (123.15 K).

To measure the joint conductance, the polymer specimen was placed between the two flux meters. Air was allowed into the air cylinder until the experimental stack (upper flux meter, specimen, lower flux meter) was vertically aligned with the specimen in light contact with both flux meters. It was desired to measure the joint resistance at cryogenic temperatures so that only the microscopic resistance at the colder interface of the specimen was considered. Dow Corning 340 heat sink compound was applied between the upper flux meter and the upper warmer specimen interface allowing the contact resistance at the upper specimen interface to be negligible.

Once the experimental stack was correctly aligned, air was allowed into the air cylinder until the desired starting apparent pressure

of 138 kPa (20 psi) was acting on the polymer specimen. The liquid nitrogen was then allowed to circulate through the lower chiller block. The temperatures through the flux meters were measured and recorded using a National Instruments (NI) SCXI hardware and NI Lab View data acquisition setup.

Because it was desired to know the joint-conductance values as a function of apparent pressure, the pressure on the polymeric specimens was varied. For the specimen the joint conductance was measured at 138-kPa increments (20 psi) from 137.9–689.5 kPa (20–100 psi) and then at 689, 1034, 1379, 2758, and 4137 kPa (100, 150, 200, 400, and 600 psi).

To obtain a joint-conductance measurement, the specimen was allowed to settle at the desired pressure for a minimum of one hour. The circulating liquid nitrogen causes a pulsating action through the chiller block; therefore, steady state was achieved when the specimen's average temperature did not change by more than $\pm 0.5^{\circ}$C over a 30-min period. Once sufficient time had been allowed for the system to reach steady state, the data acquisition was stopped, and the joint-conductance values were averaged over a 15-min period. Next, the pressure inside the air cylinder was increased until the next desired pressure was reached. The process was repeated until the final apparent pressure of 4137 kPa (600 psi) ws reached.

Experimental Calculations

The thermocouples placed in the Al flux meters were used to calculate the heat flux into and out of the polymer specimen. The temperature at each thermocouple location was recorded, and then a sum of least-squares method was used to calculate the warm and cold polymer interface temperatures. The interface temperatures were averaged to obtain an average specimen temperature.

The joint conductance was experimentally calculated by defining the joint conductance, given by Eq. (13), and Fourier's law, Eq. (14):

$$h_{j,\text{exp}} = q_{\text{flux}}/(T_{\text{us}} - T_{\text{ls}}) \tag{13}$$

$$q_{\text{flux}} = k_{\text{flux}}(\Delta T_{\text{flux}}/\Delta x_{\text{flux}}) \tag{14}$$

where T_{us} and T_{ls} are, respectively, the temperatures at the upper surface and lower surface of the two aluminum flux meters with Teflon in the middle.

The thermal conductivity of the flux meter K_{flux} was calculated by averaging the six thermocouples in the flux meter and inputting the calculated average temperature into the equation for the thermal conductivity of Al as a function of temperature (Fig. 18). To reduce the experimental uncertainty, the temperature difference ΔT_{flux} was defined by the difference in the temperature between the thermocouple at location one and the thermocouple at location six (Fig. 17). Finally, Δx_{flux} was defined as the distance between the thermocouples at location one and six, respectively.

Uncertainty Analysis

The techniques set forth by Kline and McClintock[26] were used to determine an overall experimental uncertainty of the measured joint-conductance values. The uncertainties of the various values used to calculate the joint conductance were combined to determine an overall experimental uncertainty. The total average uncertainty was calculated using the following equation:

$$\delta R = \sqrt{\sum_{i=1}^{n} \left(\frac{\partial R}{\partial x_i} \delta x_i \right)^2} \tag{15}$$

where δR is defined as the total average uncertainty for the experimental value in question.

The uncertainty of the experimentally measured joint conductance values consisted of the uncertainty in the thermal conductivity of the 6061 Al flux meters, the temperatures recorded within the flux meters, the measured distance between the thermocouple locations, and the calculated upper and lower interface temperatures across the specimens.

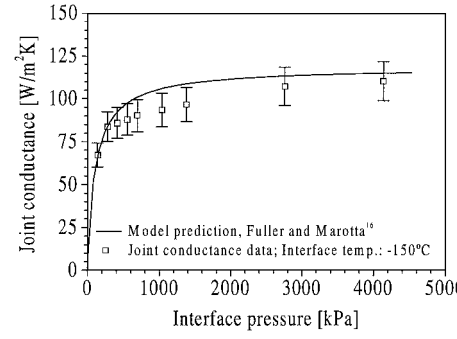

Fig. 19 Comparison of experimental data and model at cryogenic temperature (− 150°C interface temperature) as a function of interface pressures.

The uncertainty of the thermal conductivity of the 6061 Al flux meters comprised the following: the thermal conductivity of the NIST iron flux meters (3%), the temperature gradient within the NIST flux meters (2%), the temperature gradient within the Al test specimen (5%), and the measured distance between the thermocouple locations within both the NIST flux meters and the Al test specimen (1.6%). The uncertainty of the thermal conductivity of the 6061 Al flux meters was calculated to be 6.7%.

The total average uncertainty of the experimental joint-conductance values was 10.4%. The experimental uncertainty was from calculation of the temperature gradient through the Al flux meters (5.7%), the thermal conductivity of the Al flux meters (6.7%), and the measured distance between the thermocouple locations in the flux meters (0.8).

Experimental vs Model Comparison

A comparison between the experimentally gathered data for Teflon at a cryogenic interface temperature of -150°C (123.15 K) vs the model predictions of Fuller and Marotta[17] is shown in Fig. 19. The comparison is quite favorable with the model predicting the trend of the experimental data correctly. This is very interesting because this experimental study provides evidence that the polymer/metal joint model developed by Fuller and Marotta can also be applied at cryogenic temperatures. However, although the model does a good job at the two extremes, low and high pressures, within the transition region there exists a noticeable difference.

Temperature Prediction of PCR Stages Using Experimental Joint-Conduction Data

Figures 20 and 21 show the comparison between experimental data, obtained from Couto and Mantelli,[16] and theoretical data considering the experimental values of the Teflon/Metal joint, presented in this paper.

The low-conductance support used in the experimental model was bonded to each other by means of an epoxy adhesive so that the resulting interface pressure between the stages and the support is approximately 1000 kPa. This pressure was achieved by employing a calibrated weight while the adhesive cured. The values of the experimental joint conductance were obtained from Fig. 19. The value of $h_j = 90$ W/m^{2}K (corresponding to the interface pressure of 1000 kPa) was used in the comparison. This comparison is shown in Fig. 20. Also the comparison for $h_j = 75$ and 100 W/m^{2}K is shown in Fig. 21. Figures 20 and 21 show that there exists little difference in the temperature prediction using the theoretical model for this variation of h_j, which corresponds to an overall support conductance ranging from 0.0016 to 0.0020 W/m^{2}K.

In Analysis of the Sensitivity Coefficients section it was shown that the temperatures of the PCR stages are not sensitive to variations in the overall conductance within this range. The temperature becomes sensitive when the overall conductance of the support is greater than 0.01 W/m^{2}K.

The comparison between experimental data and model predictions for the cold plate and third-stage data is quite favorable,

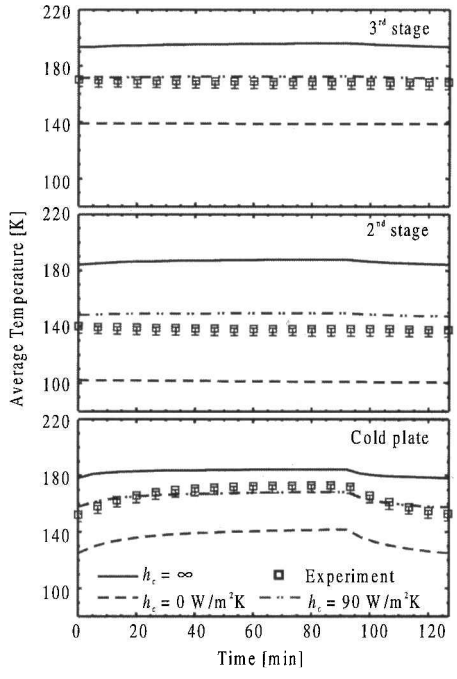

Fig. 20 Comparison between experimental data, obtained from Couto and Mantelli,[16] and theoretical predictions for an experimental value of h_j = 90 W/m²K.

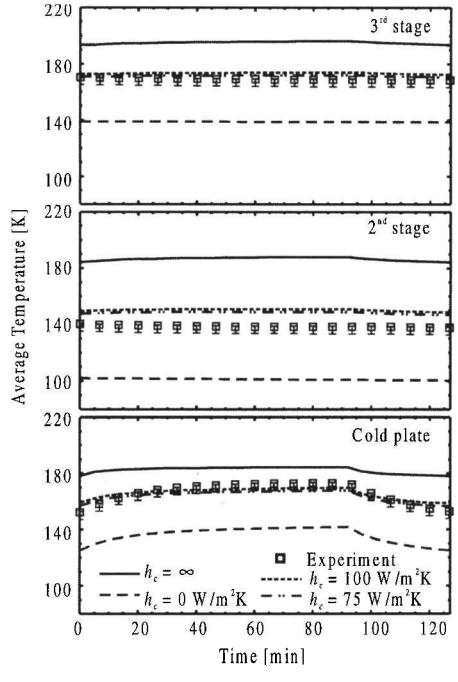

Fig. 21 Comparison between experimental data, obtained from Couto and Mantelli,[16] and theoretical predictions for experimetal values of h_j = 75 and 100 W/m²K.

whereas for the second stage it is not as accurate. The explanation for this effect is that two of the three supports in the second stage were loose, probably because of differential expansion of the Teflon support and epoxy adhesive at low temperatures, as observed after the end of the experiment. Figure 21 shows that the temperatures of the stages are not significantly affected by the joint conductance for pressure interfaces varying in the range between 200 kPa ($h_j \sim 75$ W/m²K) and 2000 kPa ($h_j \sim 100$ W/m²K).

Couto and Mantelli[16] compared experimental data with a theoretical temperature, obtained from the average of two extreme constants values of joint conductance ($h_c = 0$ and ∞ W/m²K). In this work the theoretical values for the temperature of the stages were obtained using $h_j = 90$ W/m²K (shown in Fig. 20). The deviation between these two cases is 2.97% for the cold plate. For the second and third stages the deviations are, respectively, 4.03 and 2.92%. This shows that the assumption of an average between the extreme cases is valid.

The optimum design of PCR requires the use of supports with a minimum overall conductance. For the data presented here, the lowest joint conductance is observed at pressures below 200 kPa. On the other hand, low interface pressures could not provide the mechanical coupling required by the device during the launch/ascent phases of the mission. One alternative is the heat switch presented by Milanez and Mantelli,[2] which presents a variable joint conductance. During the launch/ascent phase, the mechanical and thermal coupling is high. After thermal stabilization at low temperature in orbit, the differential expansion of the two different metals (aluminum/titanium) provides both a low thermal and mechanical coupling effect.

Conclusions

A parametric analysis of a multistage passive cryogenic radiator was described. The thermal joint conductance between Teflon polymer in contact with aluminum metal under cryogenic temperatures was successfully measured. The experimental setup for determining the joint conductance was described, and the uncertainty analysis showed that the experimental data have good accuracy at the cryogenic temperature investigated. From the results presented, some conclusions can be made:

1) The radiative and conductive insulation between the stages plays an important role in the determination of the temperature level of the stages. It is shown that the lowest values of the global conductance and effective emissivity are not always the best values. An optimum value must be obtained for each design, depending on the equipment heat load to be irradiated by the cold plate, and on the environmental heat loads, in which the spacecraft operates.

2) The surface emissivity of the stages affects almost in the same magnitude the temperature level of the stages. In this case the highest value of the surface emissivity is desirable.

3) The equipment heat loads affect the cold plate in a higher magnitude than the other stages. As the equipment heat load is a design parameter (the IR or the CCD cameras have their own and fixed heat dissipation), the designers should play with the other parameters presented in this paper.

4) The experimental data concerning the joint conductance were used as an input parameter for the mathematical model presented by Couto and Mantelli,[16] which predicts the temperature level of the stages of a passive cryogenic radiator. The theoretical results obtained by the authors, using experimental data for the joint conductance, showed good agreement with the theoretical prediction for the triple-stage passive cryogenic radiator modeled by Couto and Mantelli,[16] considering the average value of the two extreme contact cases (perfect and no contact). Experimental investigations of PCR temperature behavior should be performed when the supports employed exhibit very low joint conductance.

The data presented here are useful for future designs of passive cryogenic radiators. The Satellite Thermal Control Laboratory is also investigating other concepts of passive thermal control devices at cryogenic temperature levels, such as cryogenic heat pipes.

Acknowledgments

Couto and Mantelli would like to acknowledge the Brazilian Space Agency—AEB, CAPES Foundation, and Brazilian Council of Research and Development—CNPq, for supporting this project. Fuller and Marotta would like to acknowledge Ochterbeck and Peterson for the use of the liquid nitrogen cryogenic apparatus employed in this study.

References

[1] Hulett, R. H., and Ziermann, C. A., "Staged Radiator Design for Low Temperatures Spacecraft Applications," *Progress in Astronautics and Aeronautics*, Vol. 24, edited by J. W. Lucas, MIT Press, Cambridge, MA, 1991, pp. 614–629.

[2]Milanez, F. H., and Mantelli, M. B. H., "A New Passive Heat Switch Conception for Space Applications," American Society of Mechanical Engineers, Paper NHTC99-0267, June 1999.

[3]Abrosimov, A. I., Baryshev, O. V., Khoronenko, V. A., Kosorotov, M., Lobanov, A., Paramonov, A., and Parfentiev, M., "Diode Cryogenic Heat Pipe for SODART Telescope Silicon Detector Cooling," *Proceedings of the 8th International Heat Transfer Conference*, Beijing, 1992, pp. P54/1–P54/4.

[4]Blanchard, L. E., and Weinstein, O., "Design of the Thematic Mapper," *IEEE Transactions on Geosciences and Remote Sensing*, Vol. GE-18, No. 2, 1980, pp. 147–160.

[5]Brand, O., and Schlitt, R., "Low Temperature Radiator Design for the ABRIXAS X-Ray Satellite," *Proceedings of the 6th European Symposium on Space Environmental and Control Systems*, edited by T.-D. Guyenne, 1997, pp. 151–159.

[6]Merrian, R., and Gabron, F., "Spaceborne Passive Radiators for Detector Cooling," American Society of Mechanical Engineers, Paper 71-Av-30, May 1972.

[7]Amidieu, M., and Maciaszek, T., "Development of Fluid Loops and Hybrid Radiators Test Results," *Proceedings of the 4th European Symposium on Space Environmental and Control Systems*, edited by T. D. Guyenne and J. J. Hunt, ESA, Publ. SP-324, Vol. 2, 1991, pp. 735–740.

[8]Gilmore, D. G., *Satellite Thermal Control Handbook*, Aerospace Corp. Press, El Segundo, CA, 1994, pp. 8/17–8/25.

[9]Wright, J. P., and Pence, W. R., "Development of a Cryogenic Heat Pipe Radiator for a Detector Cooling System," American Society of Mechanical Engineers, Paper 73-ENAs-47, July 1973.

[10]Wright, J. P., "Development of a 5 W 70 K Passive Radiator," AIAA Paper 80-1512, July 1980.

[11]Wilson, D. E., and Wright, J. P., "The Multistage Heat Pipe Radiator—An Advancement in Passive Cooling Technology," AIAA Paper 77-760, June 1977.

[12]Wilson, D. E., and Wright, J. P., "Development and Testing of Two- and Three-Stage Heat Pipe Radiator," AIAA Paper 79-1060, June 1979.

[13]Couto, P., and Mantelli, M. B. H., "Cryogenic Systems for Spacecraft Applications," *Proceedings of the 7th Brazilian Congress of Engineering and Thermal Sciences*, edited by S. L. Braga, Rio de Janeiro, Brazil, 1998, pp. 1089–1094 (original version in Portuguese).

[14]Beck, J. V., Blackwell, B., and St. Clair, C. R., *Inverse Heat Conduction—Ill Posed Problems*, Wiley-Interscience, New York, 1985, pp. 19–35.

[15]Couto, P., "Development and Design of Passives Cryogenic Radiators for Spacecraft Applications," M.S. Thesis, Mechanical Engineering Dept., Federal Univ. of Santa Catarina, Florianopolis, SC, Brazil, July 1999 (original version in Portuguese).

[16]Couto, P., and Mantelli, M. B. H., "Transient Temperature Behavior of Multistage Cryogenic Radiators: Model and Experimental Validation," *Journal of Thermophysics and Heat Transfer*, Vol. 14, No. 3, 2000, pp. 313–321.

[17]Fuller, J. J., and Marotta, E. E., "Thermal Contact Conductance of Metal/Polymer Joints," *Journal of Thermophysics and Heat Transfer*, Vol. 14, No. 2, 2000, pp. 283–286.

[18]Mikic, B. B., "Thermal Contact Conductance; Theoretical Considerations," *International Journal of Heat and Mass Transfer*, Vol. 17, 1974, pp. 205–214.

[19]Mayer, R. D., "Fabrication of a Lightweight Circular Orbit Passive Radiative Cooler," Philco-Ford-Corp., Palo Alto, CA, March 1972.

[20]Gayrard, J., "SIGMA VCHP Radiator: In Orbit Performance," *Proceedings of the 4th European Symposium on Space Environment and Control Systems*, edited by T. D. Guyenne and J. J. Hunt, ESA, Publ. SP-324, Vol. 2, 1991, pp. 729–733.

[21]Beck, J. V., Cole, K. D., Haji-Sheikh, A., and Litkouhi, B., *Heat Conduction Using Green's Functions*, Hemisphere, Washington, DC, 1992, pp. 216–218.

[22]Couto, P., Mantelli, M. B. H., and Lopes, A. A., "Experimental Setup Tests for a Multistage Passive Cryogenic Radiator for Space Applications," *Proceedings of the 15th Brazilian Congress of Mechanical Engineering* [CD-ROM], Aguas de Lindoia, SP, Brazil, Nov. 1999.

[23]Marotta, E. E., and Fletcher, L. S., "Thermal Contact Conductance of Selected Polymeric Materials," *Journal of Thermophysics and Heat Transfer*, Vol. 10, No. 2, 1996, pp. 334–342.

[24]Askeland, D. R., *The Science and Engineering of Materials*, 3rd ed., PWS Publishing, Boston, 1994.

[25]Van Krevelen, D. W., *Properties of Polymers*, 3rd ed., Elsevier, Amsterdam, 1990.

[26]Kline, S. J., and McClintock, F. A., "Describing Uncertainties in Single-Sample Experiments," *Mechanical Engineering*, Vol. 75, No. 1, 1953, pp. 3–8.